Carbohydrate Polymers 104 (2014) 231–237

Contents lists available at ScienceDirect

Carbohydrate Polymers

journal homepage: www.elsevier.com/locate/carbpol

Chitosan-triphosphate nanoparticles for encapsulation of super-paramagnetic iron oxide as an MRI contrast agent

Chutimon Sanjai[a], Suchart Kothan[a,**,1], Pattarapond Gonil[b], Somsak Saesoo[b], Warayuth Sajomsang[b,*]

[a] Department of Radiologic Technology, Faculty of Associated Medical Sciences, Chiang Mai University, Chiang Mai 50200, Thailand
[b] Nanodelivery System Laboratory, National Nanotechnology Center, National Science and Technology Development Agency, Pathumthani, 10120, Thailand

ARTICLE INFO

Article history:
Received 9 November 2013
Received in revised form 1 January 2014
Accepted 3 January 2014
Available online 10 January 2014

Keywords:
Chitosan
Chitosan-TPP nanoparticles
Super-paramagnetic iron oxide nanoparticles
Encapsulation
Magnetic resonance imaging (MRI)

ABSTRACT

Super-paramagnetic iron oxide nanoparticles (SPIONPs) were encapsulated at various concentrations within chitosan-triphosphate (SPIONPs-CS) nanoparticles using an ionotropic gelation method. The encapsulation of SPIONPs within CS nanoparticles enhanced their dispersion ability in aqueous solution, with all particles being lower than 130 nm in size and having highly positive surface charge. The SPIONPs-CS nanoparticles exhibited crystalline structure and super-paramagnetic behavior, as seen in non-encapsulated SPIONPs. The morphology of SPIONPs-CS nanoparticles showed that they almost spherical in shape. The effect of phantom environments (culture medium and 3% agar solution) on either T_1 or T_2 weighted MRI was investigated using a clinical 1.5 T MRI scanner. The results revealed that 3% agar solution showed relaxation values higher than the culture medium, leading to a significant decrease in the MR image intensity. Our results demonstrated that the SPIONPs-CS nanoparticles can be applied as tissue-specific MRI contrast agents.

1. Introduction

Magnetic resonance imaging (MRI) is a non-invasive powerful three-dimensional technique for the characterization and detection of human diseases (Ernst, Bodenhausen, & Wokaun, 1990; Yan, Robinson, & Hogg, 2007). This technique has several advantages over others such as extreme imaging flexibility, non-ionizing, being harmless to patients, having high patient acceptance, giving high-resolution images with an excellent soft tissue contrast between different tissues, and allowing acquisition of unique clinical information (Stephen, Kievit, & Zhang, 2011; Shokrollahi, 2013). The main advantage of MRI is its superb spatial resolution, however the limitation of MRI in molecular imaging is in its lower sensitivity when compared to nuclear imaging. Therefore, the development of MRI contrast agents with high efficiency and sensitivity becomes essential for allowing successful bio-imaging at the cellular and molecular level.

Most clinical MRI contrast agents can be classified into two major classes based on their magnetic properties. Firstly, paramagnetic agents are composed of complexes of chelating agents and naturally occurring metal ions, with the complexes having unpaired electrons (Stephen, Kievit, & Zhang 2011; Yan, Robinson, & Hogg 2007; Lu, Salabas, & Schüth, 2007). Paramagnetic agents shorten the longitudinal relaxation time (T_1) and create bright contrast, resulting in enhanced signal intensity with positive enhancement (hyper-intensity) of T_1-weighted images. A second class is the super-paramagnetic agents, which consist of an iron oxide or Fe/Mn composite metal core covered in a polymer matrix to prevent aggregation. Super-paramagnetic agents generally have a significantly larger magnetic moment than paramagnetic agents (Burtea, Laurent, Vander Elst, & Muller, 2008; Alford, Ogawa, Choyke, & Kobayashi, 2009; Hoehn, Himmelreich, Kruttwig, & Wiedermann, 2008). Super-paramagnetic agents allow shortening of the transverse relaxation time (T_2), providing dark field in images, resulting in a decrease of signal intensity with negative enhancement (hypo-intensity) in T_2-weighted images and T_2^*-weighted images. Paramagnetic agents suffer from several disadvantages, such as a low concentration of metal ion per molecule, relative toxicity, short retention times in blood circulation, poor detection sensitivity, poor in vivo distribution, and their use creating a possible increased risk of renal dysfunction in patients (Stephen, Kievit, & Zhang, 2011; Na, Song, & Hyeon, 2009; Zhou et al., 2013). Many of these problems are not evident in super-paramagnetic agents, resulting in them being more attractive alternatives in molecular imaging applications. Super-paramagnetic iron oxide nanoparticles (SPIONPs) like Fe_3O_4 and Fe_2O_3 are widely used magnetic nanoparticle-based

* Corresponding author. Tel.: +66 2 564 7100; fax: +66 2 564 6981.
** Corresponding author.
E-mail addresses: suchart@chiangmai.ac.th (S. Kothan), warayuth@nanotec.or.th, sajomsang@hotmail.com (W. Sajomsang).
[1] Tel.: +66 5 394 9208; fax: +66 5 394 9207.

0144-8617/$ – see front matter © 2014 Elsevier Ltd. All rights reserved.
http://dx.doi.org/10.1016/j.carbpol.2014.01.012

contrast agents due to their chemical stability, biodegradability and low toxicity (Shim, Lim, & Nam, 2008; Szpak et al., 2012). However, iron oxide nanoparticles (IONPs) themselves without polymer coating or encapsulation often undergo aggregation in water or tissue fluid, which limits in vitro and in vivo magnetic-based isolation and detection strategies, as well as their usefulness in clinical MRI applications (Bonnemain, 1998; Lin, Lee, & Chiu, 2005).

Chitosan (CS), a natural cationic polysaccharide derived from chitin, has been widely used in medical applications due to its non-toxic nature, low immunogenicity, excellent biocompatibility and biodegradability. Under physiological conditions, the positively charged primary amino groups on the CS backbone can interact electrostatically with the negatively charged IONP surface, allowing CS to be utilized for coating IONPs and preventing aggregation of the IONPs, enabling their efficacy as contrast agents (Szpak et al., 2012; Lee et al., 2009; Muthiah, Park, & Cho, 2013). However, to this point less attention has been paid to the development of SPIONPs encapsulated within CS nanoparticles. In the current study, aqueous dispersions of Fe_3O_4 nanoparticles were synthesized by a co-precipitation method in the presence of sodium hydroxide under nitrogen atmosphere. Encapsulation of SPIONPs into CS nanoparticles was carried out using an ionotropic gelation method, with pentasodium triphosphate (TPP) as a cross-linking agent. The chemical structures, physicochemical properties and morphologies of SPIONPs encapsulated CS-triphosphate (SPIONPs-CS) nanoparticles were characterized using ATR-FTIR, DLS, TEM, XRD, and VSM measurements. To further investigate the potential usage of the SPIONPs-CS nanoparticles in MRI, the effect of MRI phantom media, both culture medium and 3% (w/v) agar solution, on longitudinal (T_1) and transverse (T_2) relaxation times were investigated using a clinical 1.5 T MRI scanner.

2. Materials and methods

2.1. Materials

Chitosan (CS) having an average M_W of 10 kDa and degree of deacetylation (DDA) = 96% was purchased from OilZac Technologies Co., Ltd. (Bangkok, Thailand). Anhydrous ferric chloride ($FeCl_3 \geq 98\%$) was purchased from Fluka-Chemika (Deisenhofen, Germany). Ferrous sulfate ($FeSO_4 \cdot 7H_2O$) 99.5%, sodium hydroxide (NaOH), dimethyl sulfoxide (DMSO) and glacial acetic acid were purchased from Carlo Erba Reagents, Italy. Pentasodium triphosphate (TPP) was purchased from Acros Organics, Geel, Belgium. Dialysis tubing with molecular weight (3500 Da) cut-off was purchased from Cellu Sep T1 (Membrane Filtration Products, Inc. Segiun, TX, USA). All chemicals and reagents were used without further purification. MilliQ Plus (18.2 MΩ, Millipore, Schwalbach, Germany) purified water was used to make all aqueous solutions.

2.2. Characterizations

Attenuated total reflectance Fourier transform infrared (ATR-FTIR) spectra were recorded on a Nicolet 6700 spectrometer (Thermo Company, USA) using the single bounce ATR-FTIR spectroscopy (Smart Orbit accessory) with a diamond internal reflection element (IRE) at 25 °C. X-ray diffraction (XRD) patterns were recorded on a Bruker D8 ADVANCE with CuKα radiation (λ = 1.5406 Å). Transmission electron microscope (TEM) images were obtained on a JEM-100CX II TEM operating at 120 kV. The samples were prepared onto carbon-coated copper grids and allowed to air dry before examination. Vibrating sample magnetometry (VSM) was performed on a Lakeshore Model 740H VSM Head Drive (Cryotronics, Inc., Ohio, USA). The hysteresis of the magnetization was obtained by changing outside fields (H) between -10,000 and +10,000 G and operating at 300 K. The average hydrodynamic size and distribution of the nanoparticles were determined using dynamic light scattering (DLS, Malvern Instruments Ltd. Worcestershire, U.K.). The stability of the nanoparticles in an aqueous solution (pH 6) kept in a refrigerator at 4 °C was investigated, and the change in hydrodynamic size and zeta-potential of the particles as a function of time at 25 °C was measured. The total concentrations of iron (Fe) in the nanoparticles were determined using inductively coupled plasma–optical emission spectrometry (ICP–OES) on a PerkinElmer Model ICP-Plasma-1000 instrument (PerkinElmer Inc., Massachusetts, USA).

2.3. Synthesis of SPIONPs

The SPIONPs were synthesized by a modified co-precipitation method from that reported by Wei and coworkers (Wei, Wei, Zhang, Liu, & He, 2011). Briefly, 1.62 g of $FeCl_3$ and 1.39 g of $FeSO_4 \cdot 7H_2O$ (molar ratio of Fe(III): Fe(II) at 2: 1) were dissolved in 10 mL of 12 M HCl. The solution was added dropwise to a three-necked round bottom flask containing 50 mL of 1.5 M NaOH solution at room temperature under nitrogen atmosphere, followed by stirring for 30 min. The reaction was then heated to reflux at 70 °C for 2 h. Then, the solution was cooled down with an ice water bath. The black precipitate was isolated by centrifugation at 3000 rpm for 10 min, and then washed with DI water four times. Afterwards, the black precipitate was suspended in 100 mL of DI water and sonicated using an ultrasonic bath for 30 min. The colloidal suspension thus obtained (pH ~6) was stored at 4 °C in the dark until further use.

2.4. Preparation of SPIONP encapsulated CS-triphosphate nanoparticles

SPIONP encapsulated CS-triphosphate (SPIONPs-CS) nanoparticles were prepared using an ionotropic gelation technique. Briefly, 2 mg/mL of CS stock solution was prepared by dissolving CS in 0.4% (v/v) acetic acid solution. Different volumes of the previously prepared SPIONP colloidal solutions (0.0 mL, 0.1 mL, 0.3 mL and 0.5 mL) were added into separate vials, each containing 5 mL of CS stock solution, and these were sonicated using an ultrasonic probe (Sonics, Vibra-cell, 130 W, 40 kHz, amplitude 40%, pulse on 10 s and pulse off 5 s) for 30 min while cooling in an ice bath. 2 mL of 0.60 mg/mL TPP dropwise using a syringe pump operating at a flow rate of 1 mL/min was added into each solution. The total volume of each mixture was adjusted to 7.5 mL by adding DI water except 0.5 mL of SPIONP, and the mixture stirred for 15 min. Each mixture was then sonicated again using an ultrasonic probe for 30 min while cooling in an ice bath. The nanoparticles obtained in each were filtered through 0.22 μm millipore filters. All samples were stored at 4 °C in the dark for further use. The SPIONP encapsulated CS-triphosphate nanoparticles with different volumes of the SPIONP colloidal solutions, 0.1 mL, 0.3 mL and 0.5 mL, were abbreviated to be SPIONPs-0.1-CS, SPIONPs-0.3-CS, and SPIONPs-0.5-CS, respectively. The total Fe concentrations in all samples were determined by ICP-OES (Table 1).

2.5. MRI relaxivity measurements

MRI phantoms containing the SPIONPs-CS nanoparticles having different Fe concentrations were prepared by diluting the nanoparticle solutions with both culture medium (sterile RPMI 1640 containing 10% (v/v) heat-inactivated fetal bovine serum (Gibco®, USA), and 3% (w/v) agar solution (Difco™). MR imaging and MR relaxometry were performed with a clinical 1.5 T MRI scanner (Achieva, Philips Medical Systems, Thailand) using a knee coil at room temperature. The T_1 and T_2 relaxation times were calculated by using a nonlinear regression procedure,

Table 1
Average hydrodynamic diameter, zeta-potential and polydispersity index (PDI) of CS nanoparticles and SPIONPs-CS nanoparticles with different SPIONPs concentrations at pH 6.

Nanoparticles	CS nanoparticle concentrations (mg/mL)	Particle size (nm)	PDI	Zeta potential (mV)	Total Fe concentrations (mg/L)
CS	1.33	145.47 ± 0.61	0.22 ± 0.01	37.93 ± 0.57	–
SPIONPs	–	1185.00 ± 71	0.06 ± 0.01	19.0 ± 0.40	41,247
SPIONPs-0.1-CS	1.33	128.40 ± 0.64	0.14 ± 0.01	38.87 ± 0.06	349
SPIONPs-0.3-CS	1.33	117.03 ± 0.41	0.16 ± 0.01	37.03 ± 1.16	361
SPIONPs-0.5-CS	1.33	119.43 ± 0.75	0.16 ± 0.01	35.83 ± 0.40	888

applied from OriginPro.8 software with $M_z(t) = M_0^*(1\text{-}e^{(-t/T1)})$ and $M_{xy}(t) = M_0^* e^{(-t/T2)}$, respectively (Masoudi et al., 2012). The relaxivity values (r_1 and r_2) of SPIONPs-0.5-CS nanoparticles were calculated by plotting the relaxation rates ($1/T_1$ and $1/T_2$) versus iron concentration (Jaganathan, Hugar, & Ivanisevic, 2011). The T_1-weighted image for each sample was acquired with spin-echo (SE) at various repetition times (TR) from 100 to 6000 ms with an echo time (TE) of 10 ms. Similarly, the T_2-weighted image for each sample was acquired with turbo spin-echo (TSE) by varying the TE range between 45 ms and 500 ms, while keeping the TR constant at 2000 ms. All images were processed using field of view (FOV) 150 mm, flip angle 90°, and slice thickness 3 mm. To evaluate the signal-to-noise ratio (SNR), the mean value of the MR image intensity divided by the standard deviation (SD) noise in air with region of interest (ROI) for each case, were determined.

2.6. Cytotoxicity evaluation

Cell cytotoxicities of CS, and SPIONPs-0.5-CS nanoparticles were investigated using skin fibroblast cells (ATCC: CRL-2522) by employing the MTT assay as in a previously reported procedure (Sajomsang, Ruktanonchai, Gonil, & Nuchuchua, 2009).

2.7. Statistical analysis

All experimental measurements were collected in triplicate. Values are expressed as mean ±standard deviation (SD).

3. Results and discussion

3.1. Preparation of SPIONP encapsulated CS-triphosphate nanoparticles

The SPIONP encapsulated CS-triphosphate (SPIONPs-CS) nanoparticles with different Fe concentrations were prepared using an ionotropic gelation technique. The mechanism of CS nanoparticle formation at physiological pH is based on electrostatic interactions between the protonated amine groups in CS and negatively charged anionic group in pentasodium triphosphate (TPP). Besides ionic bonding, it is known that, in aqueous environments, iron oxide surfaces are readily covered with hydroxyl groups (Cornell & Schwertmann, 2003). Therefore, adsorption of primary amino groups of CS onto the Fe_3O_4 surface via hydrogen bonding and coordinate covalent bond formation may occur, which was confirmed by ATR-FTIR. Fig. 1 shows ATR-FTIR spectra of SPIONPs, CS, and SPIONPs-CS nanoparticles. The ATR-FTIR spectrum of CS showed the presence of characteristic bands at 3357 and 3284 cm^{-1}, corresponding to O—H and N—H stretching. The band at 2875 cm^{-1} was typical of C—H stretching, while bands at 1641, 1587 and 1376 cm^{-1} were characteristic of amides I, II and III, respectively. The band at 1420 cm^{-1} was assigned to the C—H symmetrical deformation mode of the aliphatic CH_2—OH groups on the CS backbone. The bands at 1149 and 1024 cm^{-1} are due to C—O stretching of C—O—C in the monosaccharide rings. The band at 890 cm^{-1} corresponded to the C—H wagging of the glycosidic bond connecting the monosaccharides in the CS backbone (Brugnerotto et al., 2001). ATR-FTIR spectra of SPIONPs showed an absorption band at 590 cm^{-1}, corresponding to Fe—O—Fe in Fe_3O_4 (Fan et al., 2011; Li, Jiang, Huang, Ding, & Chen, 2008; Chen et al., 2012). However, this characteristic peak was shifted to 564 cm^{-1} when SPIONPs were encapsulated within CS nanoparticles. In addition, the absorption band due to N—H stretching of the amine group was shifted from 1587 cm^{-1} to 1558 cm^{-1} after encapsulation of SPIONPs. This may due to adsorption and bonding of the primary amino groups of CS onto the Fe_3O_4 surface.

The particle sizes and zeta-potential values of SPIONPs, CS, and SPIONP-CS nanoparticles in aqueous solution (pH 6) were determined using dynamic light scattering (DLS). Table 1 shows particle sizes and zeta-potential values for SPIONPs, CS, and SPIONPs-CS nanoparticles with different Fe concentrations. It was found that the particle size of SPIONPs was 1185 ± 71 nm, while the zeta-potential was 19.0 ± 0.40 mV. The large particle sizes of SPIONPs were due to aggregation of the SPIONPs in aqueous solution at pH 6. The CS nanoparticles alone had a much smaller size (145.47 ± 0.61 nm) while the particle size of SPIONP-CS nanoparticles was found to decrease with increasing Fe concentration (Fig. S1). This can be explained in terms of the interactions between the SPIONPs surface, and the CS nanoparticles via hydrogen bonding and coordinate covalent bond formation, leading to shrinking of the nanoparticles. Furthermore, the PDI values of the synthetic particles ranged from 0.111 to 0.219, indicating a narrow size distribution and good colloidal stability. The zeta-potential values were positively charged due to protonation of primary amino groups of CS nanoparticles under mild acidic conditions (pH ~6). It was found that the zeta-potential value of CS nanoparticles alone was 37.93 ± 0.57 mV while the zeta-potential values of SPIONPs-CS nanoparticles ranged from 35.83 ± 0.40 mV to 38.87 ± 0.06 mV (Fig. S2). The total Fe concentrations in SPIONP-CS nanoparticles were determined by ICP-OES. The results reveal that Fe concentration decreased after the SPIONPs was encapsulated into the

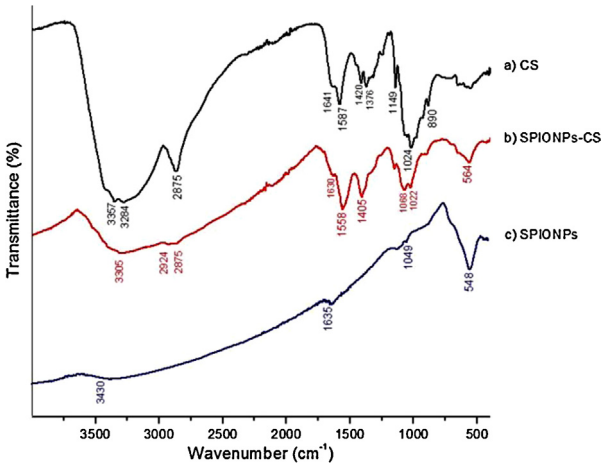

Fig. 1. ATR-FTIR spectra of CS (a), SPIONPs-0.5-CS nanoparticles (b), and SPIONPs (c).

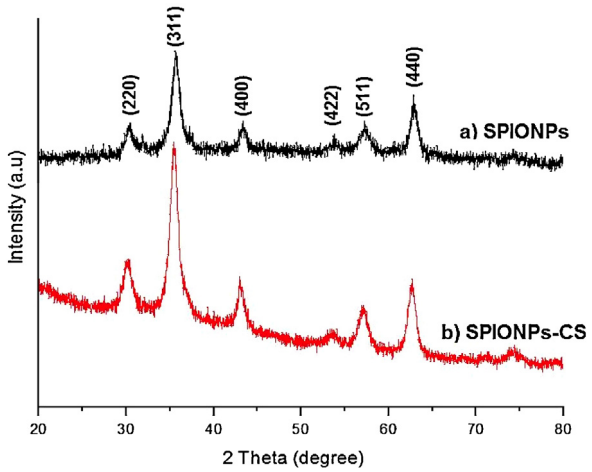

Fig. 2. XRD patterns of the SPIONPs (a) and SPIONPs-0.5-CS nanoparticles (b).

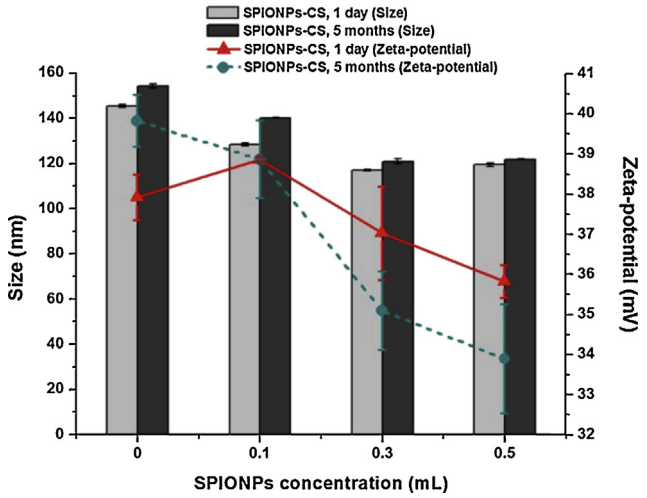

Fig. 4. Stabilities of CS nanoparticles and SPIONPS-CS nanoparticles with different SPIONPConcentrations in aqueous solution (pH = 6) for 1 day (gray), and 5 months (black). (For interpretation of the references to colour in this figure legend, the reader is referred to the web version of this article.)

CS nanoparticles. The total Fe concentrations in CS nanoparticles were found to be 349 mg/L, 361 mg/L, and 888 mg/L when 0.1 mL, 0.3 mL and 0.5 mL of aqueous dispersions of Fe_3O_4 nanoparticles were added into the CS nanoparticles, respectively (Table 1).

3.2. XRD study

The crystallinity of SPIONPs, and SPIONPs-0.5-CS nanoparticles was investigated using powder XRD, and the XRD patterns of SPIONPs and SPIONPs-0.5-CS nanoparticles are shown in Fig. 2. Six XRD diffraction peaks in SPIONPs are evident at 30.1°, 35.4°, 43.1°, 53.2°, 56.9° and 62.5° which relate to the 220, 311, 400, 422, 511, and 440 AU crystalline spinel structure of the Fe_3O_4 cubic nanocrystals (Fan et al., 2011; Schweiger, Pietzonka, Heverhagen, & Kissel 2011; Chen, Yang, Ma, & Wu, 2011; Wei et al., 2011; Li et al., 2008; Chen et al., 2012). In comparison to the SPIONPs, the SPIONPs-0.5-CS nanoparticles showed a similar XRD pattern, indicating that encapsulation did not result in any phase changes, or affect the crystalline structure of the SPIONPs.

3.3. TEM characterization

The morphology of SPIONPs-0.5-CS nanoparticles was characterized using TEM imaging (Fig. 3). Basically, the native SPIONPs tend to aggregate owing to their large specific surface area, high surface energy and magnetization effect. After being encapsulated within CS nanoparticles, the dispersibility of the SPIONPs increased significantly, a desirable feature for their use in biomedical applications. They appeared to be roughly spherical in shape and the SPIONPs are well encapsulated within the CS nanoparticles. As shown in the TEM images, the particle size of SPIONPs-0.5-CS nanoparticles were found to be 10.78 ± 1.44 nm. Notably, an outer shell of CS nanoparticles on the SPIONP surface after encapsulation could not be observed which might be due to the monolayer structure and/or thin shell formation.

3.4. Stability and VSM study

The stability of SPIONPs is one of the most important factors governing their effective utility in medical applications. Ideally, SPIONPs used in medical applications should be of narrow size distribution and show good dispersibility in aqueous solution. However, as indicated previously SPIONPs without polymer coatings, or surface encapsulation may tend to aggregate in aqueous environments, which may limit in vitro magnetic-based isolation and detection strategies, as well as their effectiveness in clinical MRI applications (Cheng et al., 2005). The stability of CS nanoparticles, and SPIONP-CS nanoparticles in aqueous solution (pH 6, kept at 4 °C) was investigated by measuring the change in particle size and zeta-potential as a function of time at 25 °C (Fig. 4). The CS nanoparticles, and SPIONP-CS nanoparticles were shown to be highly stable in aqueous solution (pH 6), with only a slight increase in size over 5 months while SPIONPs alone were unstable and observed to precipitate within a few hours. However, zeta-potential values of CS nanoparticles and SPIONPs-CS nanoparticles

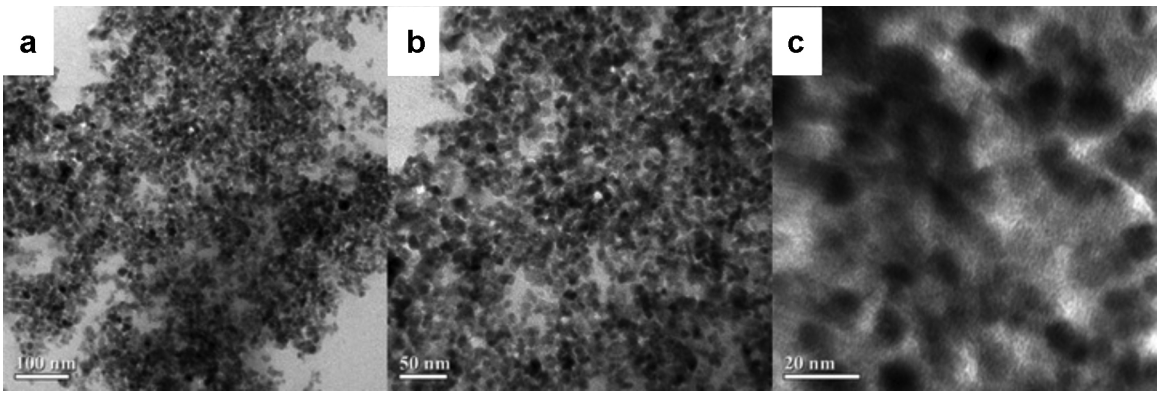

Fig. 3. TEM images of SPIONPs-0.5-CS nanoparticles with scale bar; 100 nm (a), 50 nm (b) and 20 nm (c).

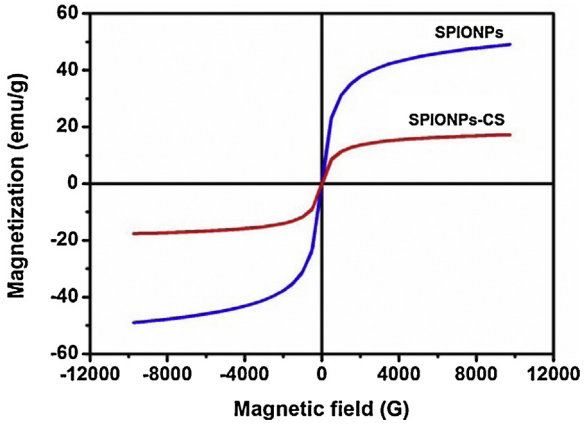

Fig. 5. Magnetization curves of SPIONPs and SPIONPs-0.5-CS nanoparticles.

decreased significantly with increasing incubation times. These results revealed that the encapsulation system used in this study can significantly reduce aggregation of SPIONPs under aqueous conditions.

The SPIONPs, and SPIONPs-0.5-CS nanoparticles were freeze dried to a solid prior to investigating their room temperature magnetic properties using VSM. The magnetic hysteresis loop characterizes the responses (magnetization) of magnetic materials to an external magnetic field. It shows that super-paramagnetic particles do not retain any magnetism after removal of the magnetic field. Therefore, they show an absence of hysteresis, much stronger magnetization, zero remanence, and zero coercivity (Mathew & Juang, 2007; Karimi, Shokrollahi, & Karimi, 2013). Fig. 5 shows a typical plot of magnetization versus applied magnetic field. Both synthesized SPIONPs and SPIONPs-0.5-CS nanoparticles show super-paramagnetic behavior, as evidenced by the zero coercivity and remanence on the magnetization loops. The saturation magnetization of SPIONPs was found to be 49 emu/g, although this significantly decreased to 17 emu/g after encapsulation within CS nanoparticles. The results revealed that encapsulation of SPIONPs within CS nanoparticles can result in significant reductions in saturation magnetization, due to the decrease of the SPIONP content in the CS nanoparticles. Furthermore, the decrease of saturation magnetization per unit mass in the SPIONPs-0.5-CS nanoparticles may be due to the increased mass of these particles in comparison with the pure SPIONPs (Qu, Shao, Jing, & Huang, 2013).

3.5. MRI relaxivity

The relaxation times were measured using a clinical 1.5 T MRI scanner to investigate the MRI signal enhancement of SPIONPs-0.5-CS nanoparticles in both culture medium, and 3% agar solution on either T_1 or T_2 weighted MRI. The efficiency of an MRI contrast agent is often exclusively studied in aqueous solution, even if the relaxation behavior in vivo is sometimes different than under in vitro conditions. Therefore, agar solution was used as a phantom medium in this study to measure the efficiency of SPIONPs-0.5-CS nanoparticles as contrast agent in a tissue-like environment, as compared to the culture medium (Gossuin, Gillis, Hocq, Vuong, & Roch, 2009). In comparison to the culture medium (Fig. 6a), 3% agar solution showed a strong decrease in signal intensity in T_2 weighted images (Fig. 7a), while the signal intensity in T_1 weighted images increased with increasing Fe concentration from 0.06 to 0.50 mM (Figs. 6a and 7a). It is important to note that at higher Fe concentration (1.0 mM), the T_1 weighted signal intensity was seen to exhibit a decrease (Fig. 7a), which could be due to the strong decrease in spin–spin relaxation rates of water molecules (R_2^*) (Xiao et al., 2011). However, the potential for both T_2 and T_1 weighting at reasonable concentrations is apparent (Cheng et al., 2005; Xiao et al., 2011). The results revealed that SPIONPs-0.5-CS nanoparticles have effects on both T_1 and T_2 relaxation times, and these depended on Fe concentrations and phantom media conditions. There are large differences in T_2 and T_1 weighted images signal intensities in 3% agar solution in comparison to when culture medium was used. Therefore, our results indicated that the SPIONPs-0.5-CS nanoparticles can be used as tissue-specific agents, in comparison to blood pool agents. A potential MRI contrast agent is usually evaluated based on its relaxivity values (r_1 and r_2) (Gossuin et al., 2009). The r_1 and r_2 values were calculated from the slopes of each plot by plotting the relaxation rates (reciprocal values of relaxation

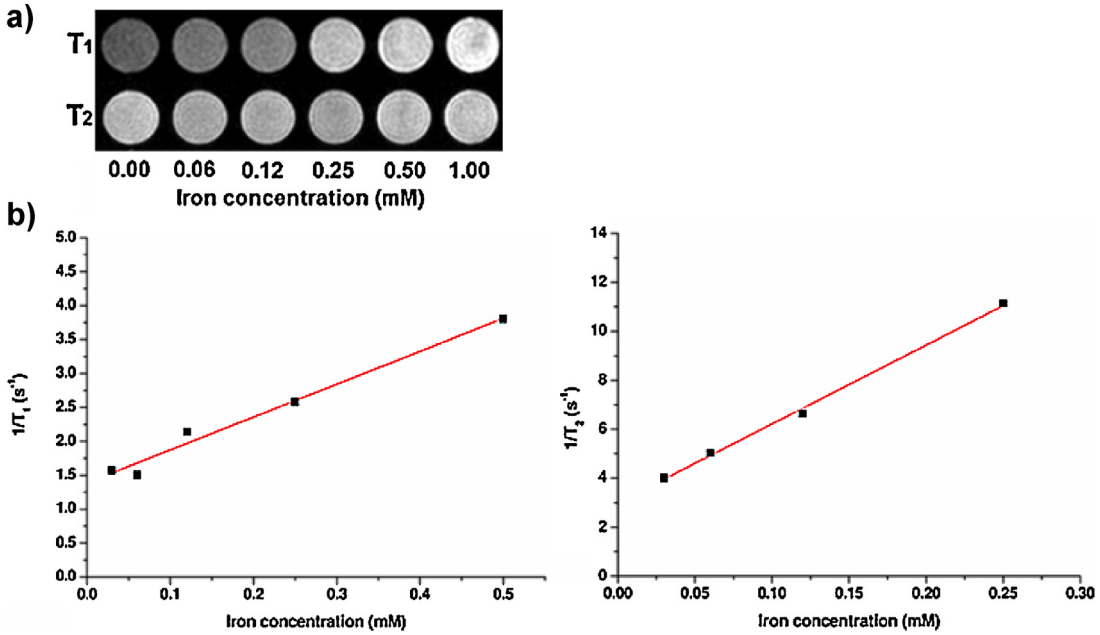

Fig. 6. MRI characterization of SPIONPs-0.5-CS nanoparticles. (a) T_1 weighted and T_2 weighted MRI results from culture medium containing SPIONPs-0.5-CS nanoparticles with different iron concentrations. (b) Plots of $1/T_1$ and $1/T_2$ against different iron concentrations in SPIONPs-0.5-CS nanoparticles.

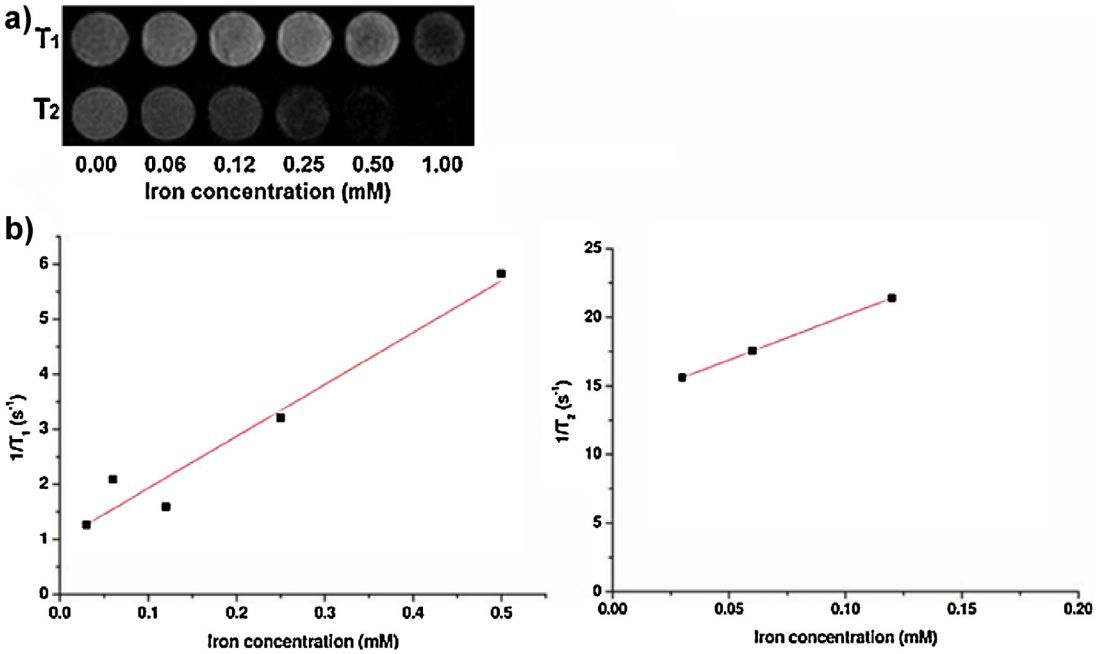

Fig. 7. MRI characterization of SPIONPs-0.5-CS nanoparticles. (a) T_1 weighted and T_2 weighted MRI results from 3% agar solution containing SPIONPs-CS nanoparticles with different iron concentrations. (b) Plots of $1/T_1$ and $1/T_2$ against different iron concentrations in SPIONPs-0.5-CS nanoparticles.

times) against Fe concentrations in the SPIONPs-0.5-CS nanoparticles (Figs. 6b and 7b). The relaxation values were determined to be $r_1 = 4.85 \pm 0.37\ mM^{-1}\ s^{-1}$ and $r_2 = 32.25 \pm 1.13\ mM^{-1}\ s^{-1}$, and $r_1 = 9.44 \pm 1.17\ mM^{-1}\ s^{-1}$ and $r_2 = 64.31 \pm 0.03\ mM^{-1}\ s^{-1}$ for culture medium and 3% agar solution, respectively (Table 2). The relaxation values in 3% agar solution were much higher than those of culture medium however the r_2/r_1 values were not significantly different in both phantom media. The r_2/r_1 values ranged from 6.65 to 6.81, suggesting their efficacy as a T_2 contrast agent having a dark effect on MRI images. Basically, induction of a magnetic field by SPIONPs perturbs the magnetic relaxation processes of the protons in the surrounding water molecules, leading to the shortening of the spin–spin relaxation time of the proton (Dastru, Longo, & Aime, 2011). Therefore, protons in the surrounding water molecules in different phantom media would be affected differently on MR images, with the effect related to the relaxation values. This is the reason why 3% agar solution showed higher relaxation values than the culture medium. These results suggested that the SPIONPs-CS nanoparticles predominantly shorten T_2 relaxation times more than T_1 relaxation times, with a decrease of MR image intensity.

3.6. In vitro cytotoxicity

Fig. 8 shows the MTT assay results for the cytotoxicity of SPIONPs-0.5-CS nanoparticles against skin fibroblast cells in comparison to native CS nanoparticles. The results revealed that increasing concentrations of CS and SPIONPs-0.5-CS nanoparticles correlated with decreasing percentages of cell viability. However, native CS nanoparticle concentrations and CS nanoparticle concentrations in SPIONPs-0.5-CS ranging from 0.65 to 2.60 μg/mL, the cell viability of the SPIONPs-0.5-CS nanoparticles was minimally affected (80% cell viability), indicating that SPIONPs-0.5-CS nanoparticles exhibited a low cytotoxicity towards skin fibroblast cells at these concentrations. At similar CS nanoparticle concentrations, the SPIONPs-0.5-CS nanoparticles contain iron concentration ranging from 433 μg/mL to 1735 μg/mL, calculating from Table 1. It is important to observe that the SPIONPs-0.5-CS nanoparticles caused a more marked decrease in cell viability than native CS nanoparticles when concentration of CS in SPIONPs-0.5-CS nanoparticles was 5.21 μg/mL (iron concentration = 3478 μg/mL, calculating from Table 1) (Fig. 8). This is due to the strong positive charged density on the CS nanoparticles surface, and this result is in good agreement with those previously reported by Nasti et al. (Nasti et al., 2009). Therefore, at proper concentrations (0.65 to 2.60 μg/mL), SPIONPs-0.5-CS nanoparticles can be useful as a contrast agent for MRI.

Table 2
The relaxivity data of SPIONPs-0.5-CS nanoparticles as a representative T_2 contrast agent.

Phantom condition	r_1 ($mM^{-1}\ s^{-1}$)	r_2 ($mM^{-1}\ s^{-1}$)	r_2/r_1
Culture medium	4.85 ± 0.37	32.25 ± 1.13	6.65
3% Agar solution	9.44 ± 1.17	64.31 ± 0.03	6.81

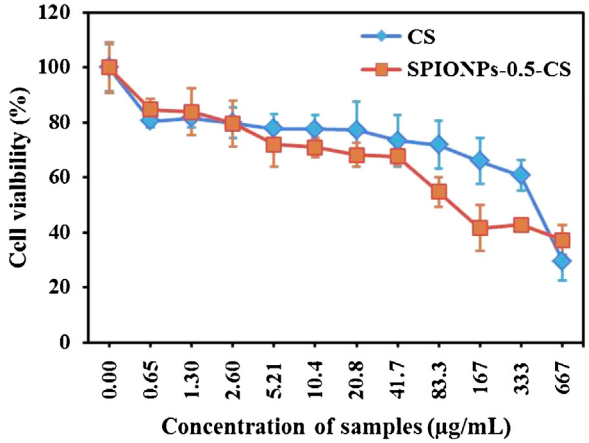

Fig. 8. Cytoxicity of CS and SPIONPs-0.5-CS nanoparticles on skin fibroblast cells following 24 h incubation as determined by MTT assay.

4. Conclusions

In summary, SPIONPs-CS nanoparticles were prepared by using an ionotropic gelation technique, with the prepared nanoparticles being less than 130 nm in size. This system has advantages over other MR agents in that preparation is simple, and can be undertaken under mild conditions. Furthermore, SPIONPs-CS nanoparticles showed low cytotoxicity against skin fibroblast cells at proper concentrations, and excellent stability for over prolonged periods. The SPIONPs-CS nanoparticles exhibited superparamagnetic properties at room temperature and possessed r_2/r_1 values between 6.65 and 6.81, suggesting that these are T_2 contrast agents for MR imaging. The SPIONPs-CS nanoparticles in 3% agar solution showed relaxation values higher than in culture medium, and in both cases predominantly shortened T_2 relaxation times compared to T_1 relaxation times were observed. Our results demonstrated that SPIONPs-CS nanoparticles have the potential to be utilized as a MR contrast agents in tissue environments in the human body.

Acknowledgments

C. Sanjai particularly thanks the National Research University Project under Thailand's Office of the Commission of Higher Education (CHE) for finance support and gratefully acknowledges the National Nanotechnology Center (NANOTEC), National Science and Technology Development Agency (NSTDA), Thailand.

Appendix A. Supplementary data

Supplementary data associated with this article can be found, in the online version, at http://dx.doi.org/10.1016/j.carbpol.2014.01.012.

References

Alford, R., Ogawa, M., Choyke, P. L., & Kobayashi, H. (2009). Molecular probes for the in vivo imaging of cancer. *Molecular BioSystem*, *5*, 1279–1291.

Bonnemain, B. (1998). Superparamagnetic agents in magnetic resonance imaging: Physicochemical characteristics and clinical applications. *Journal of Drug Targeting*, *6*, 167–174.

Brugnerotto, J., Lizardi, J., Goycoolea, F. M., Argüelles-Monal, W., Desbrières, J., & Rinaudo, M. (2001). An infrared investigation in relation with chitin and chitosan characterization. *Polymer*, *42*, 3569–3580.

Burtea, C., Laurent, S., Vander Elst, L., & Muller, R. N. (2008). Contrast agents: Magnetic resonance. *Handbook of Experimental Pharmacology*, *185*, 135–165.

Cheng, F. Y., Su, C. H., Yang, Y. S., Yeh, C. S., Tsai, C. Y., Wu, C. L., Wu, M. T., & Shieh, D. B. (2005). Characterization of aqueous dispersions of Fe_3O_4 nanoparticles and their biomedical applications. *Biomaterials*, *26*, 729–738.

Chen, J. P., Yang, P. C., Ma, Y. H., & Wu, T. (2011). Characterization of chitosan magnetic nanoparticles for in situ delivery of tissue plasminogen activator. *Carbohydrate Polymers*, *84*, 364–372.

Chen, X., Lv, H., Ye, M., Wang, S., Ni, E., & Zeng, F. (2012). Novel superparamagnetic iron oxide nanoparticles for tumor embolization application: Preparation, characterization and double targeting. *International Journal of Pharmaceutics*, *426*, 248–255.

Cornell, R. M., & Schwertmann, U. (2003). *The iron oxides: Structure, properties, reactions, occurrences and uses* ((2nd ed.)). Weinheim: Wiley-VCH Verlag GmbH & Co. KGaA.

Dastru, W., Longo, D., & Aime, S. (2011). Contrast agents and mechanisms. *Drug Discovery Today: Technologies*, *8*, e109–e115.

Ernst, R. R., Bodenhausen, G., & Wokaun, A. (1990). *Principles of nuclear magneticr-Resonance in one and two dimensions*. New York: Oxford University Press.

Fan, C., Gao, W., Chen, Z., Fan, H., Li, M., & Deng, F. (2011). Tumor selectivity of stealth multi-functionalized superparamagnetic iron oxide nanoparticles. *International Journal of Pharmaceutics*, *404*, 180–190.

Gossuin, Y., Gillis, P., Hocq, A., Vuong, Q. L., & Roch, A. (2009). Magnetic resonance relaxation properties of superparamagnetic particles. *Wiley Interdisciplinary Reviews: Nanomedicine and Nanobiotechnology*, *1*, 299–310.

Hoehn, M., Himmelreich, U., Kruttwig, K., & Wiedermann, D. (2008). Molecular and cellular MR imaging: Potentials and challenges for neurological applications. *Journal of Magnetic Resonance Imaging*, *27*, 941–954.

Jaganathan, H., Hugar, D. L., & Ivanisevic, A. (2011). Examining MRI contrast in three-dimensional cell culture phantoms with DNA-templated nanoparticle chains. *ACS Applied Materials and Interfaces*, *3*, 1282–1288.

Karimi, Z., Shokrollahi, H., & Karimi, L. (2013). Nano-magnetic particles used in biomedicine: Core and coating materials. *Materials Science & Engineering C*, *33*, 2465–2475.

Lin, C. L., Lee, C. F., & Chiu, W. Y. (2005). Preparation and properties of poly(acrylic acid) oligomer stabilized superparamagnetic ferrofluid. *Journal of Colloid and Interface Science*, *291*, 411–420.

Lee, M., Jeong, H. J., Kim, S. L., Kim, E. M., Kim, D. W., & Lim, S. T. (2009). SPION-loaded chitosan-linoleic acid nanoparticles to target hepatocytes. *International Journal of Pharmaceutics*, *371*, 163–169.

Li, G. Y., Jiang, Y. R., Huang, K. L., Ding, P., & Chen, J. (2008). Preparation and properties of magnetic Fe_3O_4-chitosan nanoparticles. *Journal of Alloys and Compounds*, *466*, 451–456.

Lu, A. H., Salabas, E. L., & Schüth, F. (2007). Magnetic nanoparticles: Synthesis, protection, functionalization, and application. *Angewandte Chemie International Edition*, *46*, 1222–1244.

Masoudi, A., Madaah Hosseini, H. R., Seyed Reyhani, S. M., Shokrgozar, M. A., Oghabian, M. A., & Ahmadi, R. (2012). Long-term investigation on the phase stability, magnetic behavior, toxicity, and MRI characteristics of superparamagnetic Fe/Fe-oxide core/shell nanoparticles. *International Journal of Pharmaceutics*, *439*, 28–40.

Mathew, D. S., & Juang, R. S. (2007). An overview of the structure and magnetism of spinel ferrite nanoparticles and their synthesis in microemulsions. *Chemical Engineering Journal*, *129*, 51–65.

Muthiah, M., Park, I. K., & Cho, C. S. (2013). Surface modification of iron oxide nanoparticles by biocompatible polymers for tissue imaging and targeting. *Biotechnology Advances*, *31*, 1224–1236.

Nasti, A., Zaki, N. M., de Leonardis, P., Ungphaliboon, S., Sansongsak, P., Rimoli, M. G., & Tirelli, N. (2009). Chitosan/TPP and chitosan/TPP hyaluronic acid nanoparticles: Systematic optimization of the preparative process and preliminary biological evaluation. *Pharmaceutical Research*, *26*, 1918–1930.

Na, H. B., Song, I. C., & Hyeon, T. (2009). Inorganic nanoparticles for MRI contrast agents. *Advanced Materials*, *21*, 2133–2148.

Qu, J. B., Shao, H. H., Jing, G. L., & Huang, F. (2013). PEG-chitosan-coated iron oxide nanoparticles with high saturated magnetization as carriers of 10-hydroxycamptothecin: Preparation, characterization and cytotoxicity studies. *Colloids and Surfaces B: Biointerfaces*, *102*, 37–44.

Sajomsang, W., Ruktanonchai, U. R., Gonil, P., & Nuchuchua, O. (2009). Mucoadhesive property and biocompatibility of methylated *N*-aryl chitosan derivatives. *Carbohydrate Polymers*, *78*, 945–952.

Schweiger, C., Pietzonka, C., Heverhagen, J., & Kissel, T. (2011). Novel magnetic iron oxide nanoparticles coated with poly(ethylene imine)-g-poly(ethylene glycol) for potential biomedical application: Synthesis, stability, cytotoxicity and MR imaging. *International Journal of Pharmaceutics*, *408*, 130–137.

Shim, S. Y., Lim, D. K., & Nam, J. M. (2008). Ultrasensitive optical biodiagnostic methods using metallic nanoparticles. *Nanomedicine*, *2*, 215–232.

Shokrollahi, H. (2013). Contrast agents for MRI. *Materials Science and Engineering C*, *33*, 4485–4497.

Stephen, Z. R., Kievit, F. M., & Zhang, M. (2011). Magnetite nanoparticles for medical MR imaging. *Materials Today*, *14*, 330–338.

Szpak, A., Kania, G., Skorka, T., Tokarz, W., Zapotoczny, S., & Nowakowska, M. (2012). Stable aqueous dispersion of superparamagnetic iron oxide nanoparticles protected by charged chitosan derivatives. *Journal of Nanoparticle Research*, *15*, 1–11.

Wei, X., Wei, Z., Zhang, L., Liu, Y., & He, D. (2011). Highly water-soluble nanocrystal powders of magnetite and maghemite coated with gluconic acid: Preparation, structure characterization, and surface coordination. *Journal of Colloid and Interface Science*, *354*, 76–81.

Xiao, L., Li, J., Brougham, D. F., Fox, E. K., Feliu, N., Bushmelev, A., Schmidt, A., Mertens, N., Kiessling, F., Valldor, M., Fadeel, B., & Mathur, S. (2011). Water-soluble superparamagnetic magnetite nanoparticles with biocompatible coating for enhanced magnetic resonance imaging. *ACS NANO*, *5*, 6315–6324.

Yan, G. P., Robinson, L., & Hogg, P. (2007). Magnetic resonance imaging contrast agents: Overview and perspectives. *Radiography*, *13*, e5–e19.

Zhou, Z., Wang, L., Chi, X., Bao, J., Yang, L., & Zhao, W. (2013). Engineered iron-oxide-based nanoparticles as enhanced T_1 contrast agents for efficient tumor imaging. *ACS Nano*, *7*, 3287–3296.